

LES of the flow around a finite-length square cylinder with free-end slot suction

Zeng Lingwei¹⁾, *Wang Hanfeng²⁾ and Peng Si³⁾

^{1), 2), 3)} *Department of Civil Engineering, Central South University, Changsha, China*

ABSTRACT

Large Eddy Simulation (LES) is used to study the influence of free-end steady slot suction on the aerodynamic forces and flow around a three-dimensional finite-length square cylinder with a square cross-section. Flow structure around the cylinder has been compared systematically for the suction coefficient $Q = 0, 1$ and 3 . Special attention is paid on the flow around the free end of the cylinder. Suction coefficient Q is defined as $Q = U/U_\infty$, where U is the velocity in the exit of the slot suction, U_∞ is the oncoming flow velocity. We find that the free-end steady slot suction can effectively suppress the aerodynamic forces of the model. The Controlling result is the best when $Q = 1$. Relative to the none control case, mean drag, fluctuating drag and fluctuating lift are decreased by 3.75%, 19.08%, 40.91%, respectively. The mean negative pressure and fluctuating pressure on the free end are most significant at $Q = 1$, which enhances the upwash flow along with cylinder side faces and the momentum exchange between free-end shear flow and near wake flow. Thus, it effectively suppresses the spanwise vortex shedding and the aerodynamic forces of the cylinder. In this paper, we focus on flow field characteristics to explain the control mechanism of the steady slot suction at the free end. Source point and flow reattachment separation occur at the top of the model when $Q = 1$. Flow reattachment has not happened at the plane of $y = 0$ but occurs symmetrically on both sides of the top. In addition, according to the λ_2 criterion, we find that when $Q = 0$ and 3 , the wake structure of $\lambda_2 = 0.4$ iso-surface presents as a continuous structure, while when $Q = 1$, the wake structure is broken and discontinuous.

Keywords: aerodynamic forces; finite-length square cylinder; steady suction; flow control; large eddy simulation

1. INTRODUCTION

Flow around wall-mounted finite-length cylinders (WMFLC) is frequently encountered in engineering applications, e.g. high-rise building, chimney, etc. The flow around

²⁾ Professor
^{1,3)} Graduate Student

a finite-length cylinder is highly three-dimensional (3D) and drastically different from that around a two-dimensional (2D) one (Park & Lee 2000; Sumner et al. 2004; Wang & Zhou 2009; Krajnovic 2011; Sattari et al. 2012; Kawai et al. 2012; Wang et al. 2017). Particularly, the flow around a WMFLC is characterized by tip vortices or trailing vortices, spanwise vortices and possible base vortices (Wang and Zhou. 2006; Wang and Zhou. 2009; Kawai et al. 2012). Both tip vortices and base vortices induce downwash and upwash flow in spanwise direction, which tend to weaken the periodic spanwise vortex shedding (Porteous et al. 2014; Wang et al. 2016). The base vortices and associated upwash flow depend on the boundary layer condition where the WMFLC mounted. The base vortices will be enhanced with the increase of boundary layer thickness on the bottom wall (Wang et al. 2006). The spanwise vortices depend largely on the cylinder aspect ratio H/d , where H and d are the height and width of the cylinder, respectively. When H/d falls below a critical value, the spanwise vortex changes from staggered arranged to symmetrically arranged (Sakamoto & Arie 1983; Okamoto & Sunabashiri 1992; Pattenden et al. 2005). Sakamoto & Arie (1983) suggested that this critical value is 3.0 for a circular finite-length cylinder and 2.5 for square one.

Based on time-averaged near wake velocity field, Tanaka & Murata (1999) calculated the mean vortex line downstream a finite-length circular cylinder with $H/d = 1.25$ and 10. They found the vortices from both sides of the cylinder are connected with each other near the free end, forming an arch-type structure. Wang & Zhou (2009) performed flow visualization in the spanwise and lateral planes simultaneously for the flow around a finite-length square cylinder with $H/d = 7$. They found that, from the instantaneous point of view, the spanwise shear flow and free-end shear flow are also connected with each other forming an arch-type structure. Kawai et al. (2012) confirmed this observation using 3D stereoscopic PIV measurement for a finite-length square cylinder with $H/d = 2.7$.

High-rise building can be considered as typical wall-mounted finite-length cylindrical structure. The wind induced forces and associated vibrations are generally crucial for the design of high-rise building (Gu et al. 2004; Quan et al. 2012). Shape optimization is one of the most widely used measures to reduce the wind load and wind induced vibration of high-rise buildings (Dutton et al. 1990; Choi et al. 2008; Tanaka et al. 2012; Kim et al. 2015). Kim et al. (2015) investigated the wind load of a simplified high-rise building model with a regular polygonal section,

Kim et al. (2015) investigated the wind load of a simplified high-rise building model with a regular polygonal section, e.g. triangular, square, pentagon, etc. The effects of both the number of sides n and spanwise helical were studied. They found the overturning and torsional moment decrease with increasing n , but this decrease become less pronounced when $n > 5$. Meanwhile, the optimization effects of helical also become limited $n > 5$.

A lot of investigations have been conducted on the effects of corner modification, e.g. corner recessing, chamfering and rounding, on a high-rise building with square cross section (Kawai 1998, Mandal & Faruk 2010, Tanaka et al. 2012, Carassale et al. 2014 and Li et al. 2018). Li et al. (2018) found that, for a square high-rise building model with $H/d = 8$, if its corners are replaced by chamfered ones, the RMS across-

wind base moment can be reduced by 37.5%. Other shape modifications were also tested to reduce the wind load on high-rise buildings. Dutton et al. (1990) found that through openings in the upper half of a high-rise building can significantly suppress its wind load and associated transverse wind-induced vibration. Xie (2014) found tapering or stepping along the height of a high-rise building can reduce its cross-wind aerodynamic responses. Particularly, the peak of the wind load spectrum has been significantly reduced by tapering for it may spread wind energy to a higher reduced frequency region. However, all these shape optimization methods have significant effects on the structural and architectural design for the building (Mooneghi & Kargarmoakhar 2016).

Steady suction near the spanwise leading edges of finite-length square cylinder with $H/d = 3.7$ can also reduce its mean aerodynamic drag by about 74% and effectively suppress the flow separations on the side faces (Zheng & Zhang 2012). Moreover, Menicovich et al. (2014) experimentally investigated the influence of steady tangential blowing near the spanwise leading edge of a high-rise building model on its aerodynamic performance. They suggested that the mean drag and fluctuating lift can be reduced by 14.2% and 6.1%, respectively, at the blow ratio of 2, which was defined as the ratio of the mean jet velocity measured at the orifice exit plane to the mean free stream velocity measured at the top of the model. Zhang et al. (2016) compared the effects of steady suction at different positions of a square high-rise building model with $H/d = 6$. They found the suction holes at side faces are more efficient than those at the leeward face in suppressing the aerodynamic forces. Moreover, for the suction on side faces, the control effect becomes more remarkable with the suction holes getting closer to the leading edge, where the flow separation occurs. The perturbations in all the above mentioned active controls are arranged along the spanwise direction of the cylinder, which is essentially similar to the control for 2D bluff bodies (Choi et al. 2008).

Tanaka & Murata (1999), Wang & Zhou (2009), Kawai et al. (2012), Zhang et al. (2017) show that the free-end shear flow and the spanwise shear flow around a finite-length cylinder are connected and form a closed arch type vortex structure. Therefore, it is possible to control the entire near wake flow and associated aerodynamic forces by manipulating the free-end shear flow. Park & Lee (2004) experimentally investigated the influence of free-end geometry on the near wake of a finite-length circular cylinder with $H/d = 6$. They suggested that, relative to a flap tip, the hemispherical free end can significantly weaken regular vortex shedding from the cylinder and reduce the reverse flow zone downstream the cylinder. More recently, Wang et al. (2018) found that the aerodynamic forces of a finite-length square cylinder with $H/d = 5$ can be significantly reduced by steady slot suction near its free-end leading edge. Particularly, the fluctuating lift is reduced by 45.5% with the suction ratio of 1, i.e., the suction velocity at the slot equals to the oncoming flow velocity U_∞ . Although, Wang et al. (2018) investigated the behaviors of the free-end shear flow using Cobra probe and smoke wire flow visualization for different suction ratio, the control mechanism is still not thoroughly understood yet.

In this paper, Large Eddy Simulation (LES) is used to study the influence of free-end steady slot suction on the aerodynamic forces of and flow around a finite-length square cylinder with $H/d = 5$. The Simulation results under three typical suction coefficients are compared in detail, especially the free-end shear flow. The control

mechanism of steady slot suction at the free end of a finite-length square cylinder is revealed.

2. Numerical simulation introduction

2.1 Numerical methods

The idea of LES is to disintegrate the vortex of turbulent into large scale and small scale with certain filter. According to Kolmogorov's theory, the large-scale vortices depend on the geometry which can be explicitly solved. On the other hand, the small-scale vortices are more universal whose effect is represented by sub-grid-scale (SGS) model. (Chen et al. 2009).

The Navier-Stokes (N-S) equations of incompressible fluid are shown in Eqs. 1(a & b), and the filtered N-S equations are shown in Eqs. (2 a & b).

$$\frac{\partial u_i}{\partial t} + \frac{\partial}{\partial x_j} (u_i u_j) = -\frac{\partial p}{\partial x_i} + \frac{\partial}{\partial x_j} \left[\nu \left(\frac{\partial u_i}{\partial x_j} + \frac{\partial u_j}{\partial x_i} \right) \right] \quad (1a)$$

$$\frac{\partial u_j}{\partial x_j} = 0 \quad (1b)$$

$$\frac{\partial \bar{u}_i}{\partial t} + \frac{\partial}{\partial x_j} (\bar{u}_i \bar{u}_j) = -\frac{1}{\rho} \frac{\partial \bar{p}}{\partial x_i} + \nu \frac{\partial^2 \bar{u}_i}{\partial x_j^2} - \frac{\partial \tau_{ij}}{\partial x_j} \quad (2a)$$

$$\frac{\partial \bar{u}_i}{\partial x_i} = 0 \quad (2b)$$

where ρ is the density of the fluid, ν is the kinematic viscosity coefficient of the fluid, \bar{u}_i and \bar{u}_j are the velocity after filtering, \bar{p} is the pressure after filtering, x_i , x_j are the direction components in cartesian coordinate system ($i, j = 1, 2, \text{ and } 3$), τ_{ij} is the unsolved SGS turbulent stress, where $\tau_{ij} = \overline{u_i u_j} - \bar{u}_i \bar{u}_j$. The anisotropic part of the SGS stress is represented by an eddy viscosity model:

$$\tau_{ij} - \frac{1}{3} \tau_{kk} \delta_{ij} = -2\nu_{sgs} \bar{S}_{ij} = -\nu_{sgs} \left(\frac{\partial \bar{u}_i}{\partial x_j} + \frac{\partial \bar{u}_j}{\partial x_i} \right) \quad (3)$$

in which \bar{S}_{ij} is solvable scale strain rate tensor, τ_{kk} is the isotropic part of SGS stress and is included in the filtered pressure term, δ_{ij} is the normal stress of SGS, ν_{sgs} is sublattice turbulent eddy viscosity coefficient. Smagorinsky hypothesis (Smagorinsky 1963) is adopted in this paper, which suggests $\nu_{sgs} = (C_s \Delta)^2 |\bar{S}|$, where C_s is the Smagorinsky constant, for flow around blunt bodies, $C_s = 0.1$ (Krajnovic 2002). The strain rate tensor $\bar{S} = \sqrt{2\bar{S}_{ij}\bar{S}_{ij}}$. Δ is the grid width, $\Delta = (\Delta x \Delta y \Delta z)^{1/3}$, where Δx , Δy , Δz are

the grid size in x , y , and z directions, respectively. Commercial software Fluent is utilized to conduct the numerical simulation for the present paper.

2.2 Simulation model

The width of the finite-length square cylinder $d = 40$ mm. And its aspect ratio $H/d = 5$. The computational domain and coordinate system are shown in Fig. 1(a). The origin of the coordinates is defined at the center of the test model on the bottom wall. The length, width, and height of the computational domain are $30d$, $20d$, and $10d$, respectively. The model is $10d$ downstream from the inlet of the computational domain.

There is a slot on the cylinder free end to establish a steady suction at it, as shown in Fig. 1(a). The slot is $0.025d$ downstream from the free-end leading edge. The length and width of the slot suction are $0.9d$, $0.025d$, and the depth of the slot is d , as shown in Fig. 1(a). Note that, the boundary condition of the suction slot is not defined at the cylinder free end. Instead, a velocity outlet is defined at the bottom face of the slot, as indicated by the green square face in Fig. 1(a). This definition approach for the suction slot allows the formation of secondary vortices near the entrance of slot on the cylinder free end (Raju et al. 2005 and Kotapati et al. 2007).

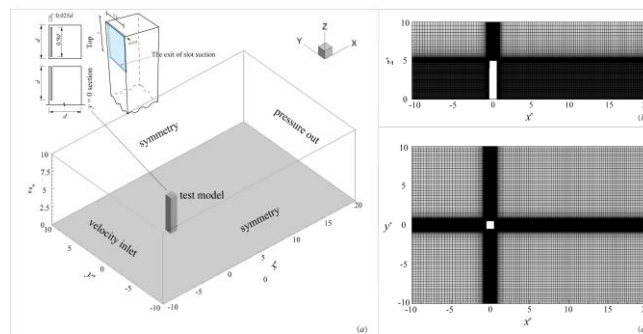


Fig. 1 Numerical simulation model and computational meshes

A uniform flow with the oncoming velocity U_∞ of 10m/s is given at the inlet of the computation domain. The Reynolds number Re based on U_∞ and d is 2.78×10^4 , which is the same as that used in Wang et al. (2018)'s experiment.

The outlet of the domain is set as pressure-out. The top and sides surfaces of the computational domain are defined as symmetry boundary condition. Besides, the surfaces of the cylinder and the bottom wall of the computational domain are set as no-slip-wall. The boundary layer thickness on the bottom wall is estimated to be about 1 mm, i.e., $0.25d$. That is most the cylinder span is immersed in uniform oncoming flow.

Suction coefficient Q is defined as U_s/U_∞ , where U_s is the velocity at the exit of the suction slot. Wang et al. (2018) experimentally investigated the effects of Q on the aerodynamic forces on a finite-length square cylinder with $H/d = 5$. They found that, relatively to the uncontrolled case ($Q = 0$), the aerodynamic forces present their minimal values at $Q = 1$. The forces recover slightly with increasing Q for $Q \geq 1$, and become almost constant for $Q \geq 3$. Consequently, the present paper studies the three typical suction ratios, i.e., $Q = 0, 1$ and 3 . To this end, the velocity at the exit of the

suction slot (see Fig. 1a), is set as 0, 10 and 30 m/s, respectively.

The Strouhal number ($= f_s \cdot d / U_\infty$, where f_s is the dominant vortex shedding frequency) of a finite-length square cylinder with $H/d = 5$ is about 0.11 (McClellan et al. 2014, Unnikrishnan & Ogunremi 2017, and Wang et al. 2018), slightly smaller than the corresponding value of 2D square cylinder. Since $U_\infty = 10$ m/s, thus the dominant spanwise vortex shedding frequency is estimated to be 27.5 Hz, and the corresponding period is 0.0364 s. The time step in the present simulation is set as 0.001 s, which is about 1/36 of the vortex shedding period.

2.3 Mesh independence verification

The computational domain is discretized into structured hexahedral mesh, as shown in Fig. 1(b). The mesh near the cylinder surface is refined in all three directions. Three sets of meshes are tested to investigate their effects on the simulation results. Table 1 lists the information of the three sets of meshes, named Case 1, 2 and 3, used for comparison. All these three sets of meshes meet the condition of $y^+ < 1$ on the model surface. The main difference of these meshes lies in the total number of the grids, which is 4 million, 7 million and 8 million in Case 1, 2 and 3, respectively.

Table 1 Comparison of different calculation cases

case	Total number	Δt	y^+
1	4×10^7	0.001	<1
2	7×10^7	0.001	<1
3	8×10^7	0.001	<1

3. Results analysis and discussion

3.1 Aerodynamic analysis

Fig. 2 shows the velocity distribution at the entrance of the slot suction for different suction coefficients Q . $\overline{U_z^*}$ ($= U_z/10$) is the dimensionless velocity in z-direction. The measurement position is dimensionless with d . The results show that when $Q = 0, 1$ and 3, except for the absolute velocity value in the middle position are larger. When $Q = 0$, $\overline{U_z^*}$ is basically at 0, when $Q = 1$, $\overline{U_z^*}$ is basically at -1, when $Q = 3$, $\overline{U_z^*}$ is basically at -3. Which ensures the uniformity of velocity in the suction slot.

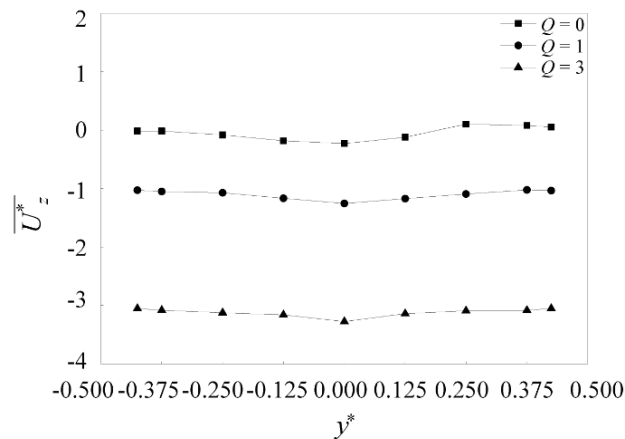


Fig. 2 Distribution of the suction velocity along the slot under different suction coefficient Q

Fig. 3 compares the results of \overline{C}_d , C'_d and C'_l obtained by LES under different suction coefficients Q and the experimental results of Wang et al (2018). It is in good agreement with the experimental results of C'_l . While, \overline{C}_d and C'_d are slightly smaller than the experimental results. The calculation results of \overline{C}_d in this paper is 1.53, while the value in Wang et al. (2018) is 1.62, and the relative error of the two is about 6%. The possible reason is that the boundary layer conditions of the simulation and the experiment are inconsistent. Although there are differences in specific values, the trends of numerical simulation results and experimental results are basically the same. All values reached to the minimum when the suction coefficient $Q = 1$. However, when $Q = 3$, all aerodynamic forces increase, but still smaller than the corresponding results when $Q = 0$. The above results show that the aerodynamic forces of the model are significantly affected by the steady slot suction near the front edge of the free end. When $Q = 1$, the weakening of aerodynamic forces is most significant. Compared with the case without suction control ($Q = 0$), \overline{C}_d , C'_d and C'_l are decreased by 3.75%, 19.08% and 40.91%, respectively.

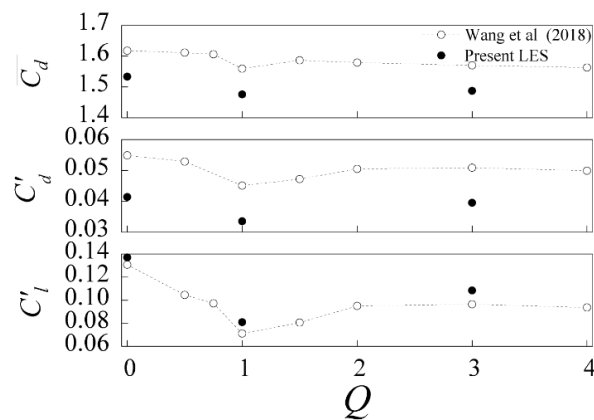


Fig. 3 Compare numerical results with Wang et al. (2018) for \overline{C}_d , C'_d and C'_l
Fig. 4 shows the distribution of the mean and fluctuating pressure coefficients, i.e.

$\overline{C_p}$ and C'_p in the side surface of the square cylinder. From the perspective of $\overline{C_p}$ distribution, $\overline{C_p}$ approximately increases from top to bottom, as shown in Fig. 4(a)-(c). The effect of suction on the distribution of C_p is not significant. However, suction control works better on the distribution of C'_p . When $Q = 1$, C'_p is markedly reduced when compared with $Q = 0$. C'_p rebound at $Q = 3$, but is still smaller than $Q = 0$, as shown in Fig. 4(d)-(f). We can conclude that suction control has an effect on the aerodynamic forces of each layer of the cylinder. When $Q = 1$, C'_p on the side surfaces has been significantly weakened.

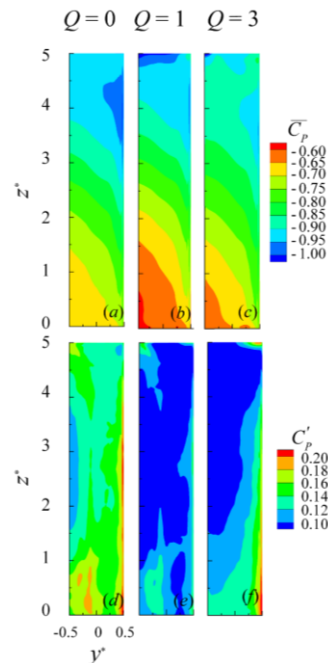


Fig. 4 Side surface mean and fluctuating pressure coefficients $\overline{C_p}$ and C'_p of the cylinder

3.2 Flow field analysis

Fig. 5 shows the time-averaged flow streamline in the plane of $y = 0$ of the square cylinder. When $Q = 0$, the oncoming flow separates at the front edge at the top of the model. Due to the negative pressure on the rear of the square cylinder, separated flow bypasses the model and forms an obvious downwash flow in its downstream. Part of the downwash flow enters the wake of the model and moves upward along the rear of the model to its free end, which forms a main vortex "V1" near the free end. The upwelling flow along the rear of the model forms a secondary vortex "V2" at the back edge of the free end, as shown in Fig. 5(a). Except for the "V2" area, the top of the model is in the reverse flow zone formed by the separation flow. When $Q = 1$, the oncoming flow still separates at the front edge, but a source point "S" appears on the free end, as shown in Fig. 5(b). Obviously, only the free end of the upstream part of source point "S" is still in the reverse flow zone. Compared with the uncontrolled condition ($Q = 0$), the free-end shear flow is significantly inclined downward under the suction of $Q = 1$. The height of the main vortex "V1" is significantly reduced. When $Q =$

3, under the strongest slot suction, the separated flow is completely inhibited. The oncoming flow is close to the free end and moves downstream. In addition, the main vortex "V1" moves further downstream, as shown in Fig. 5(c).

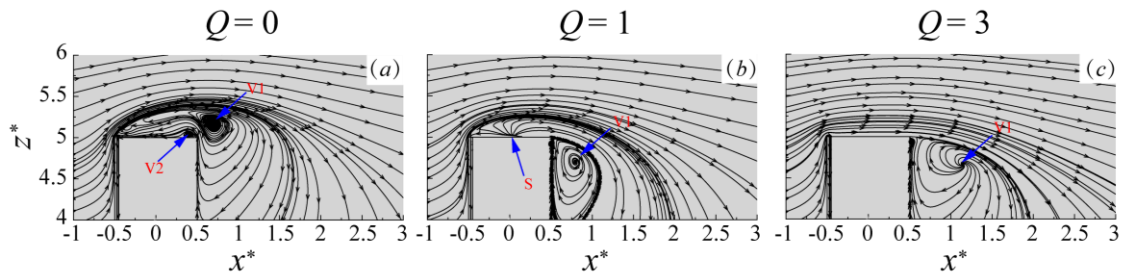


Fig.5 Time-averaged flow streamline of the model at different suction coefficients in the plane of $y = 0$

Fig. 6(a)-(c) shows the distribution of $\overline{U_x^*}$ and the time-averaged flow streamline in the plane of $y = 0$. Meanwhile, the length of the reverse flow zone is marked in red line as well as saddle point marked by red Cross. Reattachment separation phenomenon shown in **Fig. 6(b)** when $Q = 1$, while flow separation has been inhibited at $Q = 3$ shown in **Fig. 6(c)**. The reverse flow zone is 3.39 when $Q = 0$, 4.05 when $Q = 1$, 3.64 when $Q = 3$, where the starting position of the reverse flow zone is calculated on the centerline of the cylinder in the plane of $y = 0$, as shown in **Fig. 6(a)-(c)**. Compared with uncontrol condition, the length of reverse flow zone increase 19.5% when $Q = 1$, while it increases 7.4% when $Q = 3$. The saddle point of $Q = 0$ is about $0.3 d$, which is obviously smaller than **Wang & Zhou (2006)** about $1.2 d$ with a thicker boundary layer about $0.5 d$. The saddle point of $Q = 1$ is about $0.5 d$, while the saddle point of $Q = 3$ is almost the same with $Q = 0$.

Fig. 6 (d)-(e) shows the distribution of TKE^* (Turbulent Kinetic Energy) under different suction coefficients. The definition of TKE^* is given in formula 4, where, $\overline{u_x'^2}$, $\overline{u_y'^2}$, $\overline{u_z'^2}$ are the variances of velocities in the x , y and z directions, respectively. TKE^* reflects the intensity of the flow pulsation. When $Q = 1$, TKE^* is strongest in the top separation flow under $\Delta z^* \leq 0.3 d$, and its uniform distribution in the boundary layer. When $Q = 1$, the pulsation of the free end flow of the square cylinder is greatly enhanced. The strong pulsation at the top facilitates the exchange of momentum between the shear flow and the wake at the free end. As for the distribution of TKE^* in

the wake, the value of which is the strongest at $Q = 0$, followed by $Q = 3$, while $Q = 1$ is the weakest.

$$TKE^* = \frac{\overline{u_x'^2} + \overline{u_y'^2} + \overline{u_z'^2}}{2 \cdot U_\infty^2}$$

(4)

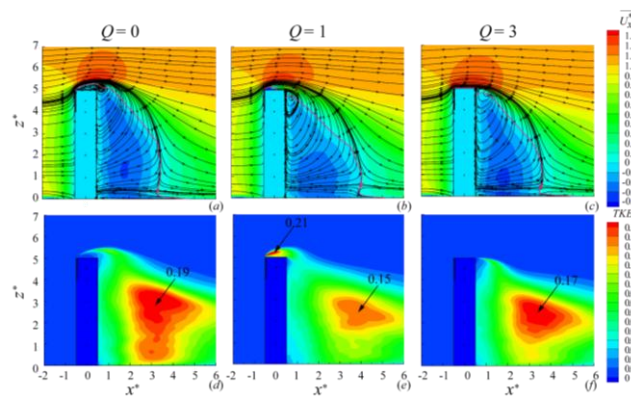


Fig. 6 Characteristics of $y = 0$ plane flow field at $Q = 0, 1$ and 3 under uniform oncoming flow: (a) time- average $\overline{U_x^*}$ distribution; (b) TKE^* distribution

Fig. 7 shows the three-dimensional streamline chart near the top of the model with different suction coefficients Q . Streamlines are colored by flow velocity. When $Q = 0$, at top of the model, a flow separation line A appears at the top of the model (as shown in **Fig. 7g**), which corresponding to line A in **Fig. 8(a)**. B and C respectively represents vortices that appear symmetrically on the sides and rear of the model. It is worth emphasizing that when $Q = 1$, under the action of the negative pressure at the top, the flows on both sides of the model will move upward along the side. Then, the flow enters into the top separation flow region, which forms two pairs of vortices D and E on the top surface, as shown in **Fig. 7(h)**. Obviously, when $Q = 1$, the flow at the top of the model is most complex, and a strong upwelling flow appears on both sides of the model. This upwelling flow will restrain the spanwise vortex shedding and weaken the aerodynamic forces of the model. When $Q = 3$, the streamline distribution is shown in **Fig. 7(i)**, where G represents the vortices that appears symmetrically on both sides of the top. The flow separation is completely inhibited in most areas at the top of the model. The streamlines are close to the top and develop downstream, as shown in region F in **Fig. 8(i)**.

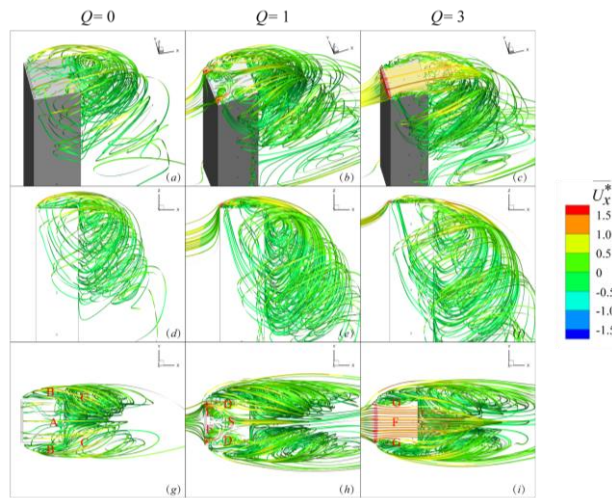


Fig. 7 Three-dimensional streamline diagram of flow field at the top under $Q = 0, 1$ and 3

In order to further study the change of free-end separation flow under different suction coefficients Q , **Fig. 8** shows the time-averaged flow field in the horizontal planes close to the top of the model. When $Q = 0$, two pairs of vortices B and C appear on both sides and downstream of the model, respectively. Where vortex C is the time-averaged result of the spanwise vortex in the wake of the model, as shown in **Fig. 8(a)**. A separation line A appears near the rear edge of the free end. Viewed from the plane of $y = 0$, this separation line A corresponds to the front side separation point of the free end trailing edge vortex "V2" in **Fig. 5(a)**. Obviously, the upstream region of the free end and separation line A are all in the reverse flow zone. When $Q = 1$, a saddle point "O" appears on the central line of the top surface, which converges the flows on the left and right sides. This saddle point "O" corresponds to the source point "S" shown in the central section in **Fig. 5(b)**. Besides, the reverse flow zone and flow close to the top surface respectively appear on the upstream and downstream of the saddle point "O", as shown in **Fig. 8(b)**. When $Q = 1$, the vortices in the wake and on the sides of the model (that is, B and C shown in **Fig. 8a**) are completely disappeared, which indicates that the spanwise vortices near the free end are significantly inhibited. When $Q = 3$, except for local area vortices on both sides of the free end, the separation flow at the front edge is completely suppressed. The oncoming flows are close to the top and develop downstream of the model, as shown in **Fig. 8(c), (f), (i)**.

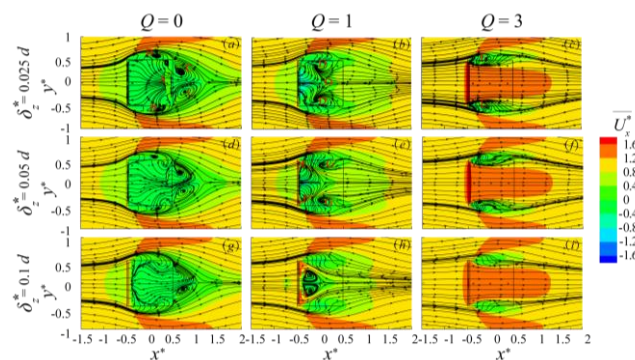


Fig. 8 Time average flow field on the top at $\delta_z^* = 0.025 d$, $0.05 d$ and $0.1 d$

Fig. 9 shows the mean and fluctuating pressure coefficients distribution on the free end of the model, i.e. $\overline{C_p}$ and C'_p . In the uncontrolled condition when $Q = 0$, $\overline{C_p}$ and C'_p on the top surface are uniformly distributed. The absolute values of $\overline{C_p}$ and C'_p are relatively small. When $Q = 1$, as the changes of flow state (as shown in Fig. 5, 8-9), $\overline{C_p}$ and C'_p distribution on the top surface also changed significantly. When $Q = 1$, a strong negative pressure region appears downstream of the slot suction, which is basically consistent with the position of top vortices D and E in Fig. 7(b). In the range of about half of the downstream of the top surface, $\overline{C_p}$ increase significantly due to flow reattachment. Meanwhile, compared with the uncontrolled condition, C'_p have been significantly enhanced near the slot suction and downstream of which, as shown in Fig. 9(e). The above phenomenon indicates that the slot suction of $Q = 1$ forms a strong negative pressure area in the front half of the free end. Which is conducive to the formation of upwelling flow on both sides of the model and thus inhibiting the spanwise vortex shedding. Strong C'_p pulsations at the top indicate that the top flow instability is most intense at $Q = 1$, which can enhance the momentum transport between the shear flow at the free end and the wake flow, thus induces stronger downwash and suppresses the spanwise vortex shedding more effectively relative to uncontrolled case, and it's further weakens the strength of wake flow. When the suction coefficient increases to $Q = 3$, the top separation flow is completely inhibited, as shown in Fig. 5, 7-8. Except for the small upstream area of the slot suction, the strong negative pressure area at the top completely disappears. Since the oncoming flow in most areas develops close to the top, the C'_p on the top also weakens significantly when $Q = 3$. The strength of slot suction is enough to completely inhibit the flow separation at the front edge of the top. $\overline{C_p}$ and C'_p at the top are significantly reduced compared with $Q = 1$. Therefore, its inhibition effect on the spanwise vortex and aerodynamic forces of the model will be correspondingly weakened.

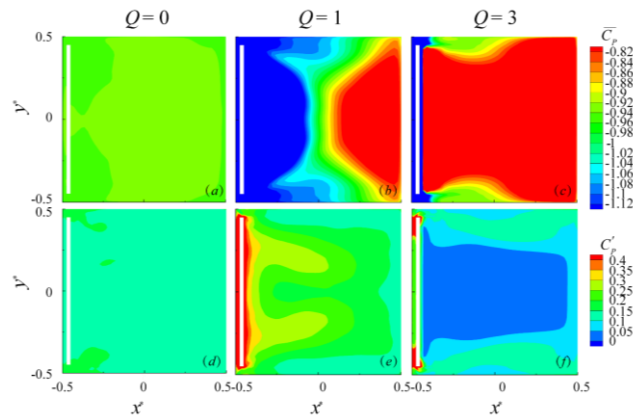


Fig. 9 Top surfaces' time-averaged pressure $\overline{C_p}$ and rms pressure C'_p of square cylinder

In order to highlight the effect of top slot suction on the wake structure of the square cylinder, **Fig. 10** shows the λ_2 iso-surface (**Zhang et al. 2017**) in the wake, which is defined as

$$\lambda_2 = 0.5(\epsilon_{ij} r_{ij} - s_{ij} s_{ij}) \quad (5a)$$

$$r_{ij} = 0.5\left(\frac{\partial u_i}{\partial x_j} - \frac{\partial u_j}{\partial x_i}\right) \quad (5b)$$

$$s_{ij} = 0.5\left(\frac{\partial u_i}{\partial x_j} + \frac{\partial u_j}{\partial x_i}\right) \quad (5c)$$

Where s_{ij} and r_{ij} are the symmetrical strain tensor and skew-symmetrical rotation tensor, respectively. Where $i, j = 1, 2$ and 3 ; u_1, u_2 , and u_3 are the velocity components along the x_1, x_2 , and x_3 directions of the cartesian coordinate system, respectively. **Fig. 10** shows the time-average iso-surface of $\lambda_2 = 0.4$ under $Q = 0, 1$, and 3 .

It can be observed in **Fig. 10(a)** that horseshoe vortices appear near the bottom plane, which is generated by the root action of the model. While the upper half of the wake is controlled by a pair of symmetrical flow vortices, namely, the top vortices. This is consistent with the phenomenon observed by **Zhang et al. 2017**. When $Q = 1$, the top

vortices of the upper half of the wake are significantly weakened. When Q increases to 3, the top vortices appear again, and its intensity is the same as the uncontrolled condition $Q = 0$. The above laws are consistent with the wind pressure and flow behavior at the top of the model. That is, when $Q = 1$, the inhibition of slot suction on the wake is the most significant.

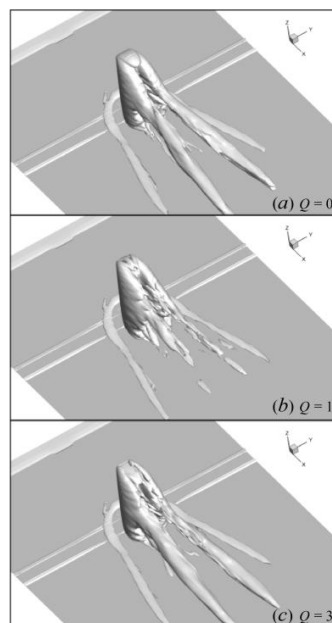


Fig. 10 Time-average iso-surface of $\lambda_2 = 0.4$

4. Conclusions

Through LES calculations, the influence of top slot suction on the flow field characteristics and aerodynamic forces of the simplified square high-rise building with $H/d = 5$ is systematically analyzed. This paper emphatically analyzes the changes of the free end shear flow under different suction coefficients Q . The following conclusions are obtained through aerodynamic force analysis, flow field analysis, and λ_2 criterion analysis.

- When $Q = 1$, the overall aerodynamic forces control effect of the model is the best. Compared with the uncontrolled condition, the mean drag, fluctuating drag and fluctuating lift are reduced by 3.75%, 19.08%, and 40.91%, respectively.
- When $Q = 1$, compared with the uncontrolled condition, the negative pressure

and pressure pulsation at the top of the model are most significant. The flows in the front half of the free end are in the separation zone. While the flows in the latter half are attached to the top surface. The top vortices in the wake are significantly weakened. Besides, when $Q = 1$, the flow separation at the top of the model is significantly inhibited, companies with the phenomenon of reattachment and separation. When suction coefficient increases to $Q = 3$, the top flow separation is completely suppressed. The strength of the top surface negative pressure and pressure pulsation are obviously weakened. The strength of the top vortices in the wake is enhanced, which is basically consistent with the uncontrolled condition.

- When $Q = 1$, the strong negative pressure on the top surface is favorable for the upwelling flow on both sides of the cylinder. This upwelling flow can effectively weaken vortex shedding of the cylinder in the spanwise direction and inhibit the aerodynamic forces of the cylinder. In addition, the strong pressure pulsation at the top enhances the momentum transport between the free end shear flow and the wake. Thus, the spanwise top vortex structure in the wake is effectively weakened.

References

- Choi, H.C., Jeon, W.P., Kim, J.S., 2008. Control of flow over a bluff body. *Annu. Rev. Fluid Mech.* 40, 113–139.
- Chen, H.L., Dai, S.S., Jia, L., Yao, X.L., 2009. Three-dimensional numerical simulation of the flow past a circular cylinder based on LES method. *J. Marine. Sci. Appl.* 8, 110-116.
- Carassale, L., Freda, A., Michela M.B., 2014. Experimental investigation on the aerodynamic behavior of square cylinders with rounded corners. *J. Fluid Struct.* 44, 195-204.
- Gu, M., Quan, Y., 2004. Across-wind loads of typical tall buildings. *J. Wind Eng. Ind. Aerod.* 92, 1147–1165.
- Kawai, H. Effect of corner modifications on aeroelastic instabilities of tall buildings. *J. Wind Eng. Ind. Aerod.* 74-76 (98), 719-729.
- Krajnovic, S., Davidson L., 2002 Large-Eddy Simulation of the Flow Around a Bluff Body. *AIAA J.* 40 (5), 927-936.
- Kim, Y.C., Kanda, J., 2010. Characteristics of aerodynamic forces and pressures on square plan buildings with height variations. *J. Wind Eng. Ind. Aerod.* 8-9 (98), 449–465.
- Krajcovic, Sinisa., 2011. Flow around a tall finite cylinder explored by large eddy

- simulation. *J. Fluid Mech.* 581, 294-317.
- Kawai, H., Okuda, Y., Ohashi, M., 2012. Near wake structure behind a 3D square prism with the aspect ratio of 2.7 in a shallow boundary layer flow. *J. Wind Eng. Ind. Aerod.* 104–106 (3), 196–202.
- Kim, Y C., Bandi, E K., Yoshida, A., Tamura, Y., 2015. Response characteristics of super-tall buildings- Effects of number of sides and helical angel. *J. Wind Eng. Ind. Aerod.* 145, 252-262.
- Li, Y., Xiang, T., Kong, F.T., Qiu, S. L., Yong, G.L., 2018. Aerodynamic treatments for reduction of wind loads on high-rise buildings. *J. Wind Eng. Ind. Aerod.* 172, 107–115.
- Mandal, A.C., Faruk, G.M.G., 2010. An experimental investigation of static pressure distribution on a group of square or rectangular cylinders with rounded corners. *J. Mech. Eng.* 41, 42–49.
- McClellan, J.F., Sumner, D., 2014. An experimental investigation of aspect ratio and incidence angle effects for the flow around surface-mounted finite-height square prisms. *J. Fluid Eng.* 136, 081206.
- Menicovich, D., Lander, D., Vollen, J., Amitay, M., Ietchford, C., Dyson, A., 2014. Improving aerodynamic performance of tall buildings using Fluid based Aerodynamic Modification. *J. Wind Eng. Ind. Aerod.* 133, 263–273.
- Mooneghi, M.A., Kargarmoakhar, R., 2016. Aerodynamic mitigation and shape optimization of buildings. *Review. J. Building Eng.* 6, 225–235.
- Okamoto, S., Sunabashiri, Y., 1992. Vortex shedding from a circular cylinder of finite length placed on a ground plane. *J. Fluids Eng.* 114, 512-521.
- Park, C.W., Lee, S.J., 2000. Free end effects on the near wake flow structure behind a finite circular cylinder. *J. Wind Eng. Ind. Aerod.* 88, 231–246.
- Park, C.W., Lee, S.J., 2004. Effects of free-end corner shape on flow structure around a finite cylinder. *J. Fluid Struct.* 19, 141-158.
- Pattenden, R.J., Turnock, S.R., Zhang, X., 2005. Measurements of the flow over a low-aspect-ratio cylinder mounted on a ground plane. *Exp. Fluid* 39, 10-21.
- Porteous, R., Moreau, D.J., Doolan, C.J., 2014. A review of flow induced noise from finite wall-mounted cylinders. *J. Fluid Struct.* 51, 240–254.

- Quan, Y., Gu, M., 2012. Across-Wind Equivalent Static Wind Loads and Responses of Super-High-Rise Buildings. *Advances in Structural Engineering*, 15(12), 2145–2155.
- Raju, R., Mittal, R., Gallas, Q., and Cattafesta, L., "Scaling of Vorticity Flux and Entrance Length Effects in Zero-Net Mass-Flux Devices." AIAA Paper 2005-4751, 2005.
- Smagorinsky, J., 1963. General circulation experiments with the primitive equations. *Mon. Weather Rev.* 91(3), 99-164.
- Sakamoto, H., Mikio, A., 1983. Vortex shedding from a rectangular prism and a circular cylinder placed vertically in a turbulent boundary layer. *J. Fluid Mech.* 126, 147-165.
- Sakamoto, H., Oiwake, S., 1984. Fluctuating forces on a rectangular prism and a circular cylinder placed vertically in a turbulent boundary layer. *J. Wind Eng. Ind. Aerod.* 106 (2), 160–166.
- Sakamoto, H., 1985. Aerodynamic forces acting on a rectangular prism placed vertically in a turbulent boundary layer. *J. Wind Eng. Ind. Aerod.* 18 (2), 131–151.
- Sumner, D., Heseltine, J.L., Dansereau, O., Dansereau, J.P., 2004. Wake structure of a finite circular cylinder of small aspect ratio. *Exp. Fluid* 37 (5), 720–730.
- Sattari, P., Bourgeois, J.A., Martinuzzi, R.J., 2012. On the vortex dynamics in the wake of a finite surface-mounted square cylinder. *Exp. Fluid* 52 (5), 1149-1167.
- Saha, A.K., 2013. Unsteady flow past a finite square cylinder mounted on a wall at low Reynolds number. *Comp. Fluid* 88(15), 599–615.
- Saeedi, M., Lepoudre, P.P., Wang, B.C., 2014. Direct numerical simulation of turbulent wake behind a surface-mounted square cylinder. *J. Fluid Struct.* 51, 20-39.
- Tanaka, S., Murata, S., 1999. An investigation of the wake structure and aerodynamic characteristics of a finite Circular Cylinder. *JSME Int. J. Ser. B: Fluids Thermal Eng.* 42 (2), 178–187.
- Tanaka, H., Tamura, Y., Ohtake, K., Nakai, M., Kim, Y.C., 2012. Experimental investigation of aerodynamic forces and wind pressures acting on tall buildings with various unconventional configurations. *J. Wind Eng. Ind. Aerodyn.* 107–108, 179–191.
- Unnikrishnan, S., Ogunremi, A., 2017. The effect of incidence angle on the mean wake

- of surface-mounted finite-height square prisms. *Int. J. Heat Fluid Flow* 66, 137-156.
- Xie, J.M., 2014. Aerodynamic optimization of super-tall buildings and its effectiveness assessment. *J. Wind Eng. Ind. Aerodyn.* 130, 88–98.
- Wang, H.F., Zhou, Y., Chan, C.K., Lam, K.S., 2006. Effect of initial conditions on interaction between a boundary layer and a wall-mounted finite-length-cylinder wake. *Phys. Fluids* 18, 065106.
- Wang, H.F., Zhou, Y., 2009. The finite length square cylinder near wake. *J. Fluid Mech.* 638, 453–490.
- Wang, H.F., Peng, S., Zhou, Y., He, X.H., 2016 a. Transition along a finite-length cylinder in the presence of a thin boundary layer. *Exp. Fluid* 57 (5), 1–10.
- Wang, H.F., Zhao, X.Y., He, X.H., Zhou, Y., 2017. Effects of oncoming flow conditions on the aerodynamic forces on a cantilevered square cylinder. *J. Fluid Struct.* 75, 140–157.
- Wang, H.F., Peng, S., Li, Y., He X.H., 2018. Control of the aerodynamic forces of a finite-length square cylinder with steady slot suction at its free end. *J. Wind. Eng. Ind. Aerod.* 179, 438–448.
- Zheng, C.R., Zhang, Y.C., 2012. Computational fluid dynamics study on performance and mechanism of suction control over a high-rise building. *Struct. Des. Tall Special Build.* 21, 475–491.
- Zhang, H., Xin, D., Ou, J., 2016. Steady suction for controlling across-wind loading of high-rise buildings. *Struct. Des. Tall Special Build.* 25, 785-800.
- Zhang, D., Cheng, L., An, H.W., Zhao, M., 2017. Direct numerical simulation of flow around a surface-mounted finite square cylinder at low Reynolds numbers[J]. *Phys. Fluids* 29, 045101.